ELSEVIER

Contents lists available at ScienceDirect

Journal of Materials Science & Technology

journal homepage: www.elsevier.com/locate/jmst



Research Article

Designing cost-performance porous thermoelectric materials by interface engineering through atomic layer deposition



Shuankui Li^{a,b,1}, Wenguang Zhao^{c,1}, Xiao-Lei Shi^{d,1}, Liangliang Wang^a, Shusheng Pan^{a,b}, Guofeng Cheng^e, Wei-Di Liu^d, Meng Li^d, Kai Guo^{a,b,*}, Zhi-Gang Chen^{d,**}, Feng Pan^{c,**}

- ^a School of Physics and Materials Science, Guangzhou University, Guangzhou 510006, China
- ^b Research Center for Advanced Information Materials (CAIM), Huangpu Research & Graduate School of Guangzhou University, Sino-Singapore Guangzhou Knowledge City, Huangpu District, Guangzhou 510555, China
- ^c School of Advanced Materials, Peking University Shenzhen Graduate School, Shenzhen 518055, China
- ^d School of Chemistry and Physics, ARC Research Hub in Zero-Emission Power Generation for Carbon Neutrality, and Centre for Materials Science, Queensland University of Technology, Brisbane, Queensland 4001, Australia
- e State Key Laboratory of High Performance Ceramics and Superfine Microstructure, Shanghai Institute of Ceramics, Chinese Academy of Sciences, Shanghai 200050, China

ARTICLE INFO

Article history: Received 21 January 2024 Revised 6 June 2024 Accepted 29 June 2024 Available online 25 July 2024

Keywords:
Thermoelectric
Bismuth telluride
Porosity
Atomic layer deposition
Interface
Performance

ABSTRACT

The bismuth-telluride-based alloy is the only thermoelectric material commercialized for the applications of refrigeration and energy harvesting, but its low cost-effectiveness severely restricts its large-scale application. The introduction of a porous structure in bulk thermoelectric materials has been theoretically proven to effectively reduce thermal conductivity and cost. However, the electrical properties of highly porous materials are considerably suppressed due to the strong carrier scattering at the interface between the matrix and pores, ultimately leading to decreased figure of merit, *ZT*. Here, we use an atomic layer deposition strategy to introduce some hollow glass bubbles with nano-oxide layers into commercial Bi_{0.5}Sb_{1.5}Te₃ for preparing high-performance porous thermoelectric materials. Experimental results indicate that the nano-oxide layers weaken carrier scattering at the interface between pores and matrix while maintaining high-strength phonon scattering, thereby optimizing carrier/phonon transport behaviors, and effectively increasing the *ZT* by 23.2% (from 0.99 to 1.22 at 350 K). Besides, our strategy has excellent universality confirmed by its effectiveness in improving the *ZT* of Bi₂Te_{2.7}Se_{0.3}, therefore demonstrating great potential for developing low-cost and high-performance thermoelectric materials.

© 2025 Published by Elsevier Ltd on behalf of The editorial office of Journal of Materials Science & Technology.

This is an open access article under the CC BY-NC-ND license (http://creativecommons.org/licenses/by-nc-nd/4.0/)

1. Introduction

More than 50% of energy consumption wastes in the form of heat [1]. Thermoelectric (TE) materials, which can directly convert heat and electricity, have attracted widespread attention [2]. The performance of TE materials is characterized by the dimensionless figure of merit, $ZT = S^2 \sigma T/\kappa = S^2 \sigma T/(\kappa_1 + \kappa_e)$, and S, σ , T, κ , κ_1 , and κ_e are the Seebeck coefficient, electrical conductivity, absolute temperature, total thermal conductivity, lattice ther-

mal conductivity, and electronic thermal conductivity, respectively [3]. Although TE technology has been commercialized for solidstate cooling [4], its widespread industrial application is still under research due to its high material cost as well as low energy conversion efficiency [5]. In the past two decades, significant progress has been achieved in improving the performance of TE materials [1]. So far, several optimization strategies, such as energy filtering [6], anisotropy enhancing (texturing) [7], defect engineering [8], and band engineering [9], have been employed to achieve highperformance TE materials. However, high material cost is another bottleneck that limits the wide application of TE technology [1]. For example, the cost of commercial p-type Bi_{0.5}Sb_{1.5}Te₃ (BST) TE materials is $\sim 8.63 \times 10^5$ \$ m⁻³ [10–12]. Therefore, it is still a big challenge to develop low-cost and high-performance TE materials, which is crucial for achieving widespread industrial applications of TE technology.

 $^{^{\}ast}$ Corresponding author at: School of Physics and Materials Science, Guangzhou University, Guangzhou 510006, China.

^{**} Corresponding authors.

E-mail addresses: kai.guo@gzhu.edu.cn (K. Guo), zhigang.chen@qut.edu.au (Z.-G. Chen), panfeng@pkusz.edu.cn (F. Pan).

¹ These authors contributed equally to this work.

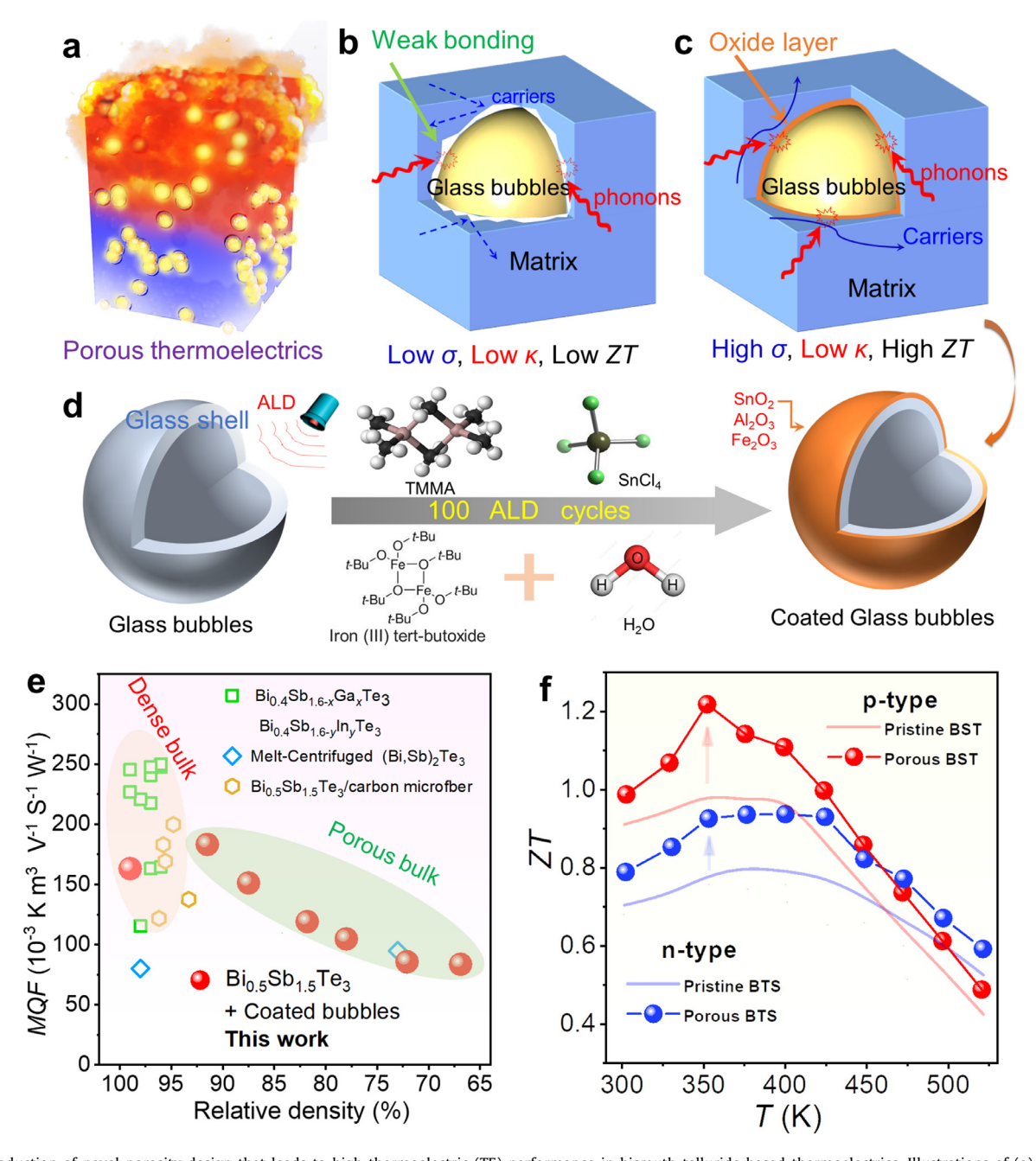


Fig. 1. Introduction of novel porosity design that leads to high thermoelectric (TE) performance in bismuth-telluride-based thermoelectrics. Illustrations of (a) a porous TE material between a temperature gradient, and glass bubbles embedded in the matrix of a TE material (b) without and (c) with bonding layers. (d) Graphical diagram of using atomic layer deposition (ALD) technique to fabricate glass bubbles with coated oxide-based bonding layers including SnO₂, Al₂O₃, and Fe₂O₃. The precursors include trimethyl aluminum, SnCl₄, iron(III) tert-butoxide (Fe₂(OtBu)₆), and H₂O. (e) Comparison of material quality factors $\mu(m^*/m_0)^{3/2}/\kappa_{latt}$ as a function of relative density between this work and reported Bi_xSb_{2-x}Te₃-based TE materials [8,32]. (f) Comparison of temperature-dependent ZTs of commercial p-type Bi_{0.5}Sb_{1.5}Te₃ (BST) and n-type Bi₂Te_{2.7}Se_{0.3} (BTS) before and after porosity designs developed by this work.

To overcome the issues of poor TE performance and high material cost, various strategies have been employed, including introducing phonon scattering centers at various scales to reduce κ_1 [13]. Among them, designing porous structures is considered an effective method to suppress the κ_1 and simultaneously reduce material costs (Fig. 1(a)). However, for highly porous materials, the κ_1 and σ may be simultaneously decreased due to phonon/carrier scattering at the interface between the matrix and pores, ultimately leading to a decrease in ZT [14]. This conclusion has been confirmed by a large number of experimental results for various porous TE materials such as Bi₂Te₃ [15], SnSe [16], PbTe [17], Cu₂Se [18], and Cu-Ni alloys [19]. For most porous TE composites, carrier

scattering at the interface between the matrix and pores may be serious due to the poor bonding, leading to significant deterioration in σ . Therefore, the decrease in κ cannot fully compensate for the severe decrease in σ , resulting in significant performance degradation of the TE materials. Literature results have shown that the material quality factors (MQFs) of dense bulk samples, defined as $\mu(m^*/m_0)^{3/2}/\kappa_1$, are relatively higher than those of porous materials. For example, for the Bi₂Te_{2.5}Se_{0.5} with a high porosity (32%), although an extremely low κ_1 of about 0.14 W m⁻¹ K⁻¹ is obtained, the MQF is only 17.3 K m³ V⁻¹ S⁻¹ W⁻¹ due to the low carrier mobility μ [20]. Similar phenomena have been widely observed in various porous TE materials, such as Bi₂Te_{2.7}Se_{0.3}/CNTs [21],

CNT/Bi₂Te₃ [20], and Cu₂Se/CNTs [22]. Therefore, carefully designing and tuning the interface between the matrix and pores is crucial for manufacturing low-cost and high-performance porous TE materials. Recently, our developed atomic layer deposition (ALD) strategy is regarded as an ideal method for designing the interface at an atomic scale, which has been successfully applied in various TE materials [23–25]. Introducing a bonding layer at the interface between the matrix and pores by the ALD technology is a promising approach for obtaining high-performance porous TE composites. The bonding layers can improve the bonding between the matrix and pores at the interface, which is likely to significantly improve carrier transport behavior while keeping strong phonon scattering at the interface (Fig. 1(b, c)), ultimately achieving a larger enhancement of ZT. Therefore, designing porous TE materials with high porosity, high σ , and low κ_1 by introducing ALD bonding layers is a promising way and worth exploring.

Based on this concept, we introduced micro-sized glass bubbles with nanoscale oxide layers into commercial TE materials to construct high-performance and low-cost TE composites. Using the ALD technique, metal oxide bonding layers were introduced at the interface between the BST matrix and glass bubbles (Fig. 1(d)). This optimization of carrier transport behavior resulted in larger MQFs and lower relative densities for the prepared porous materials (Fig. 1(e)). Porous TE materials with a relative density of \sim 86.9% achieved a high ZT of 1.22 at 350 K, showing a \sim 23.2% increase compared to solid BST (which had a ZT of 0.99 at 350 K). The TE conversion efficiency (η) was predicted using COMSOL Multiphysics based on the single-leg bulk of the prepared samples. Fig. S1 in Supporting Information shows the simulated η under different ΔTs for the pristine BST, porous BST-2%, and porous BST-8% samples. The maximum conversion efficiency (η_{max}) for porous BST-2% is 8.91%, which is approximately 10.5% higher than that of the pristine BST sample (8.06%). Additionally, for the porous BST- 8% sample, which has a low relative density of about 66.5%, a high $\eta_{\rm max}$ of approximately 6.7% is achieved, which is impressive compared to typical reported data (Fig. S1(d)) [26–31]. This strategy proved to be universally effective and can be used to design cost-effective and high-performance Bi₂Te_{2.7}Se_{0.3} (BTS)-based TE composites (Fig. 1(f)). Considering the widespread use of glass bubbles and bismuth telluride in commercial applications, this strategy holds significant commercial value and great potential for various applications.

2. Results and discussion

We used commercial BST as matrix materials, glass bubbles coated with oxide bonding layers by the ALD strategy as filler materials, and fabricated porous BST bulk materials by sintering commercial BST powders and coated glass bubbles together. To explore the suitable amount of introduced glass bubbles, we fabricated porous BST bulk materials with different nominal contents of coated glass bubbles (mass fraction, wt.%), namely 0% (no coated glass bubble added), 1%, 2%, 3%, 4%, 6%, and 8%, respectively. The coating materials were all SnO₂. The calculated and measured relative densities of as-prepared BST/glass bubble composites are shown in Fig. 2(a). The inset shows a photo of coated glass bubbles (left) and commercial BST powders (right) as raw materials for sintering, whose scanning electron microscopy (SEM) image is also shown in Fig. 2(b). Compared to the commercial BST (6.68 g cm⁻³), the glass bubbles possess a much lower density (\sim 0.6 g cm⁻³), which results in the density of the as-prepared samples sharply decreasing with increasing the content of glass bubbles. It is found that the experimental relative densities are about 10%-20% higher than the calculated values, attributed to the breakage of glass bubbles during the hot-pressing process. Fig. 2(c) shows a photo of as-sintered BST bulk materials with different

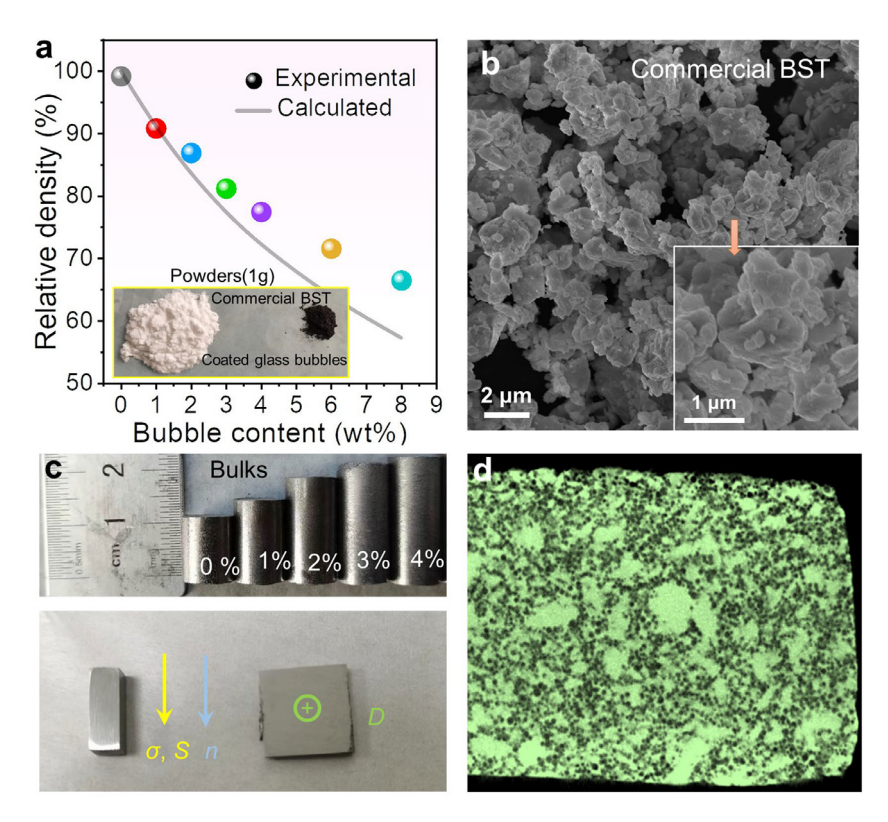


Fig. 2. Characterizations of porous Bi_{0.5}Sb_{1.5}Te₃ (BST) embedded with coated glass bubbles. (a) The calculated and measured relative densities of as-prepared BST/glass bubble composites. The inset shows a photo of coated glass bubbles (left) and commercial BST powders (right) as raw materials for sintering. (b) Scanning electron microscopy (SEM) image of the BST powders. The inset shows a corresponding magnified SEM image. (c) Photos of as-sintered BST bulk materials with different bubble contents and cut samples for evaluating their thermoelectric performance. (d) Typical Micro-XCT image for the porous BST with 8% coated glass bubbles (black: pore, green: solid phase).

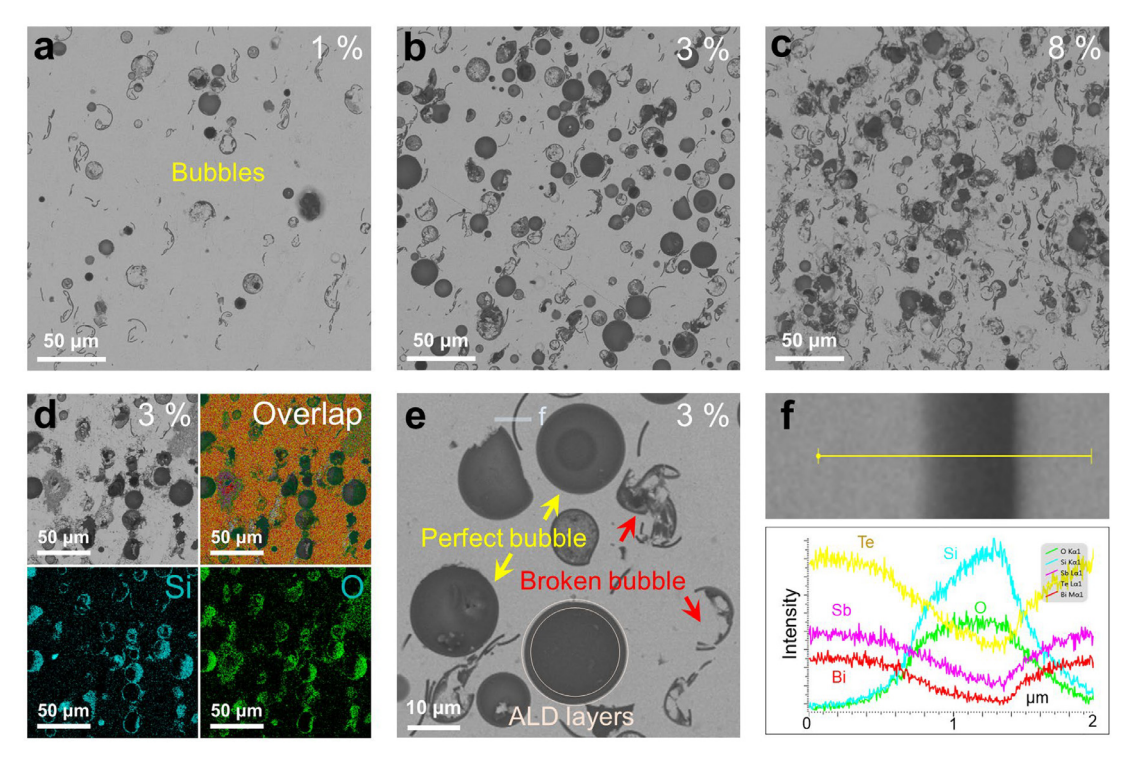


Fig. 3. Microstructural characterizations of porous BST with different contents of coated glass bubbles. SEM backscattered electron (BSE) images of polished surfaces of porous BST with (a) 1%, (b) 3%, and (c) 8% coated glass bubbles. For the sample with 3% bubbles: (d) BSE image and corresponding EDS maps for overlap, Si, and O elements. (e) Magnified SEM-BSE image. (f) High-resolution SEM-BSE image (up) and corresponding EDS line scan results (down).

bubble contents. With increasing the content of glass bubbles, the length of the sintered bulks noticeably increases. The photo of samples cut from the as-sintered BST bulk material for evaluating their performance is shown in Fig. 2(c). All the measures are operated along the direction perpendicular to the sintering pressure to ensure that the measured values are trustable. The typical micro-XCT image for the porous BST with 8% coated glass bubbles was scanned by Micro-XCT 400 (Fig. 2(d)). It is found that the glass bubbles are uniformly embedded in the BST matrix without agglomeration, as shown in Movie S1. The volume proportion of the pores in the sample is 47.6%, which is in accordance with the low relative density of about $\sim 66.5\%$.

In terms of the characterizations of as-fabricated porous BST, Fig. 3(a-c) shows backscattered electron (BSE) images of polished surfaces of porous BST with 1%, 3%, and 8% coated glass bubbles. As can be seen, for all samples, the glass bubbles are uniformly embedded in the BST matrix without agglomeration. With increasing the nominal content of bubbles, the intensity of the bubbles significantly increases in the matrix of BST. For the sample with 3% bubbles, the BSE image (Fig. 3(d)) and energy dispersive Xray spectroscopy (EDS) mapping indicate that the glass bubbles are homogeneously distributed inside the matrix (Fig. S2). Moreover, some broken glass bubbles could be observed, as shown in Fig. 3(e), which should be caused by the high pressure during the hot-pressing process although the compressive strength of the glass bubbles is as high as 193 MPa. Fig. 3(f) also shows a highresolution SEM-BSE image (up) and corresponding EDS line scan results (down) across a broken glass bubble, which reconfirms the existence of these glass bubbles. Besides, the X-ray photoelectron spectroscopy (XPS) peaks of Sn 3d and Si 2p could be detected in the as-prepared sample with 3% bubbles, confirming the successful introduction of the glass bubbles with SnO₂ layers (Fig. S3).

To further clarify the micro/nanostructural characteristics of as-fabricated porous BST, transmission electron microscopy (TEM)

characterization is employed. Fig. 4(a) presents a typical TEM image captured from the sample containing 3% SnO2-coated glass bubbles created using the focused ion beam (FIB) technique. This image reveals the presence of a characteristic porous structure. Fig. 4(b) provides another TEM image taken from the interface region shown in Fig. 4(a), highlighting the glass shell positioned between the pore and the BST matrix. The glass bubbles and BST matrix are closely fused, with the glass bubbles having a thickness of approximately 500 nm. No significant composition segregation is observed at the BST/glass bubble interface, indicating the stability of the ALD-prepared layer during the hot-pressing process. Fig. 4(c-e) exhibits high-angle annular dark-field scanning TEM (HAADF-STEM) images along with corresponding EDS maps of the Bi, Sb, Te, Si, and O elements. These images provide further evidence of the glass shell (displaying signals solely of Si and O) positioned between the pore (showing no signals) and the BST matrix. Moreover, some Sb-rich second phases are observed, which may relate to the extrusion of Te during hot press sintering. Considering that the ALD-prepared SnO2 is a typical nanoscale thin layer on the surface of the glass bubble, EDS cannot directly observe these SnO₂ layers. Fig. 4(f) shows an enlarged TEM (HRTEM) image depicting the interfaces between the BST matrix, oxide layer, and glass. The BST matrix exhibits good crystallinity. The thickness of the SnO₂ layer measures between 10 and 20 nm and is composed of nanocrystalline SnO₂. The measured interplanar spacing of the (012) planes of SnO_2 is close to the theoretical value (3.7 Å). The glass structure is typically amorphous. Fig. 4(g) is a corresponding fast Fourier transform (FFT) image. The major pattern is from the BST matrix, the minor pattern is from the nanocrystalline SnO₂, and the ring-like pattern is from the amorphous glass. Fig. 4(h) shows a magnified HRTEM image on the interface between the BST matrix and the SnO2 layer. The clear interface indicates that no composition segregation at the interface. Fig. 4(i) also shows a TEM image of a broken glass bubble in the BST matrix, which double-

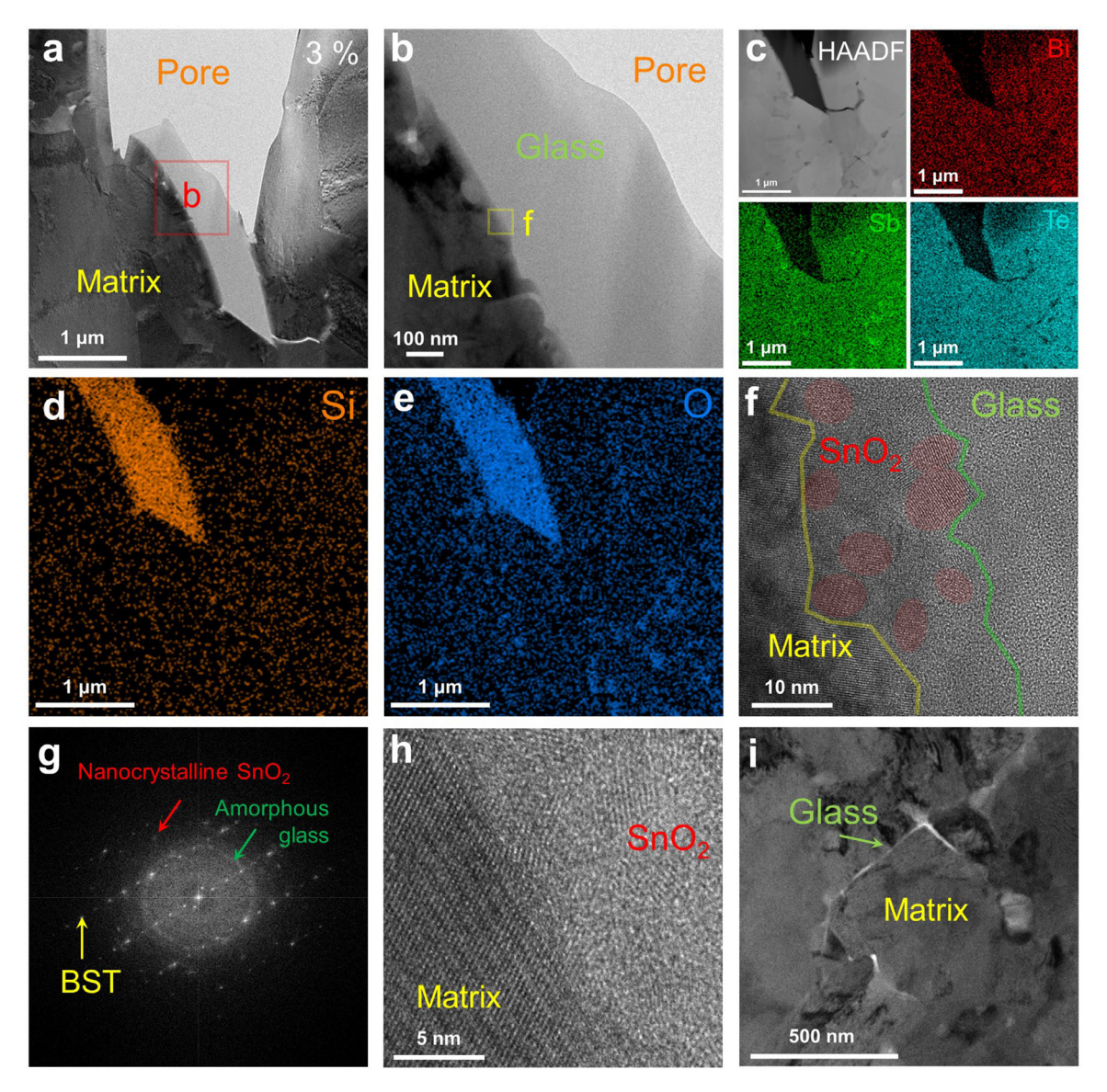


Fig. 4. Micro/nanostructural characterizations of porous BST with 3% coated glass bubbles. (a) Typical TEM image taken from the sample with 3% SnO₂-coated glass bubbles. (b) Enlarged TEM image of the red-square-circled area in (a). (c-e) HAADF-STEM image and corresponding EDS maps depicting the distribution of Bi, Sb, Te, Si, and O elements. (f) HRTEM image of the interfaces between BST matrix, SnO₂ layer, and glass. (g) Corresponding fast Fourier transform (FFT) image. (h) Magnified HRTEM image of the interface between BST matrix and oxide layer. (i) TEM image of a broken glass bubble in the BST matrix.

confirms the results observed in SEM. These results confirm that ${\rm SnO_2}$ layers guarantee the close bonding between the BST matrix and glass bubbles.

To investigate the influence of introducing coated glass bubbles on the thermal and electrical transport properties of as-prepared samples, we evaluated the TE performance of porous BST with varying contents of SnO₂-coated bubbles (0%, 1%, 2%, 3%, 4%, 6%, and 8%). Fig. 5(a-c) shows their temperature-dependent σ , S, and $S^2\sigma$. The σ of pristine BST is 789.4 S cm⁻¹ at 300 K, which is comparable to the reported BST-based material [33,34]. Notably, the σ showed a decreasing trend with increasing bubble content, attributed to carrier scattering at the interface between the BST matrix and glass bubbles. Conversely, the S remained relatively stable, as it is less sensitive to the material's structure [16]. Consequently, the $S^2\sigma$ decreased with increasing bubble content. Fig. 5(d) shows the measured hole carrier concentration $n_{\rm p}$ and μ as a function of bubble content. Both $n_{\rm p}$ and μ generally decrease with increasing glass bubble content, except for a peak in n_p when the bubble content is 1%. This behavior can be attributed to the intro-

duced porosity and the large number of interfaces. According to the EMT model, n_D and μ of porous bulk decrease by $(1-3\varepsilon/4)$, where ε is the porosity volume fraction. However, the introduced nano-oxide bonding layers may act as donor impurities, resulting in higher $n_{\rm p}$. Correspondingly, μ decreases with increasing bubble content, primarily due to the effects of porosity and the nanooxide bonding layers, which weaken carrier scattering at the interfaces between the BST matrix and glass bubbles. The effective mass m^* and deformation potential E_{def} for the as-prepared samples were calculated by a single parabolic band (SPB) model, as shown in Fig. 5(e). With increasing the nominal bubble content, the m^* decreases, and the $E_{\rm def}$ increases, except for values at 1% bubble content. The decrease in m^* indicates that the average energy of electron carriers became weaker due to the intensive scattering, while the increase in $E_{\rm def}$ ascribes to the deviation from the stoichiometry due to introducing the ALD metal oxide layer [35-37]. Therefore, the nano-oxide bonding layers are crucial to optimize the carrier transport properties of the as-prepared porous samples. Fig. 5(f) shows temperature-dependent κ . With increas-

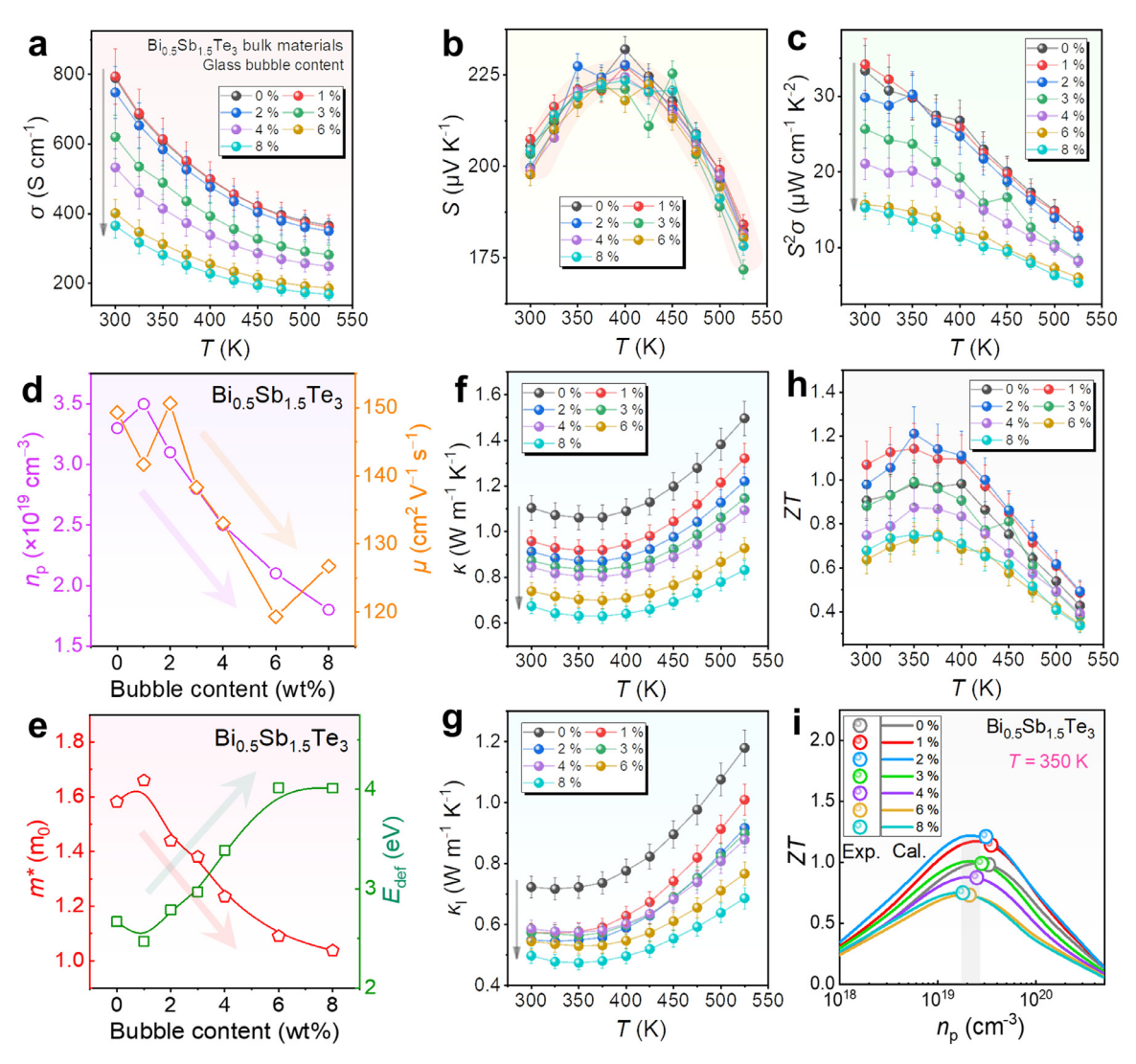


Fig. 5. Thermoelectric performance of porous BST with different contents of SnO_2 -coated bubbles (0%, 1%, 2%, 3%, 4%, 6%, and 8%). Temperature-dependent (a) σ , (b) S, and (c) power factor $S^2\sigma$. (d) Hole carrier concentration n_p and mobility μ as a function of bubble content. (e) Effective mass m^* and deformation potential E_{def} as a function of bubble content. Temperature-dependent (f) thermal conductivity κ , (g) lattice thermal conductivity κ_1 , and (h) ZT. (i) Calculated and experimental ZT as a function of n_p .

ing the nominal content of bubbles, the κ significantly reduces. Fig. 5(g) shows the κ_1 by $\kappa_1 = \kappa - \kappa_e = \kappa - L\sigma T$ [14], and the temperature-dependent κ_{e} and L calculated by an SPB model are shown in Fig. S4 for reference. Similar to the κ , with increasing the nominal content of bubbles, the κ_1 is considerably suppressed. This is because of the strengthened phonon scattering at the interfaces between the coated glass bubbles and the matrix of BST. Benefiting from the reduced κ , the peak ZT can reach 1.22 at 350 K in the sample with 2% SnO₂-coated glass bubbles, as shown in Fig. 5(h), which is comparable with other reported works as shown in Table S1 in the Supporting Information. Fig. 5(i) plots the calculated and experimental ZT at 350 K as a function of n_p , which is calculated based on the SPB model. As can be seen, the $n_{\rm p}$ is welltuned to appropriate values to achieve peak ZTs. To further improve ZT, continuing to optimize the material structure to further reduce κ should be an effective approach. Besides, our experimental results exhibit high repeatability, evidenced by Fig. S5. Moreover, the Vickers hardness for as-prepared samples with different glass bubble contents was measured by using Vickers' microhardness tester with a load of 0.1 kg and a loading time of 15 s (Fig. S6). For the sample with about 86.9% relative density, the Vickers hardness is about 82.1 HV, which is comparable with previously reported values.

To further study the effects of nano-oxide bonding layers on weakening the carrier scattering at the interfaces between the BST matrix and glass bubbles, we employed the effective medium theory (EMT) to analyze the thermal and electrical transport properties. In the case of porous materials, the conductivity $(\boldsymbol{\sigma}_{p})$ can be expressed as $\sigma_p = \sigma_d f_\sigma(\varepsilon)$ according to the EMT model. Here, the function f represents the EMT function, which depends on the porosity (ε) , and σ_p and σ_d represent the conductivity of porous and dense materials, respectively [14]. The EMT function f can be defined as $f_{\sigma}(\varepsilon) = f_{\kappa}(\varepsilon) = (1-3\varepsilon/2)$, with slight dependence on the shapes of the pores [31]. Ideally, the porosity is not expected to significantly affect the ZT values due to similar pore effects on both thermal and electrical conductivity. Fig. 6(a-c) illustrates the EMTcalculated and experimental values of σ , κ_1 , and ZT. However, the experimental data exhibit significant deviations from the curves calculated by the EMT model. In this scenario, it is necessary to consider the contributions of the glass bubbles and the BST/glass bubble interfaces. We utilize a simple mixture model to correct the EMT results based on the general rule of mixture. For the composite material, the electrical conductivity (σ_{com}) can be expressed as

$$\sigma_{\text{com}} = (1 - f)\sigma_{\text{BST}} + f\sigma_{\text{GB}} \tag{1}$$

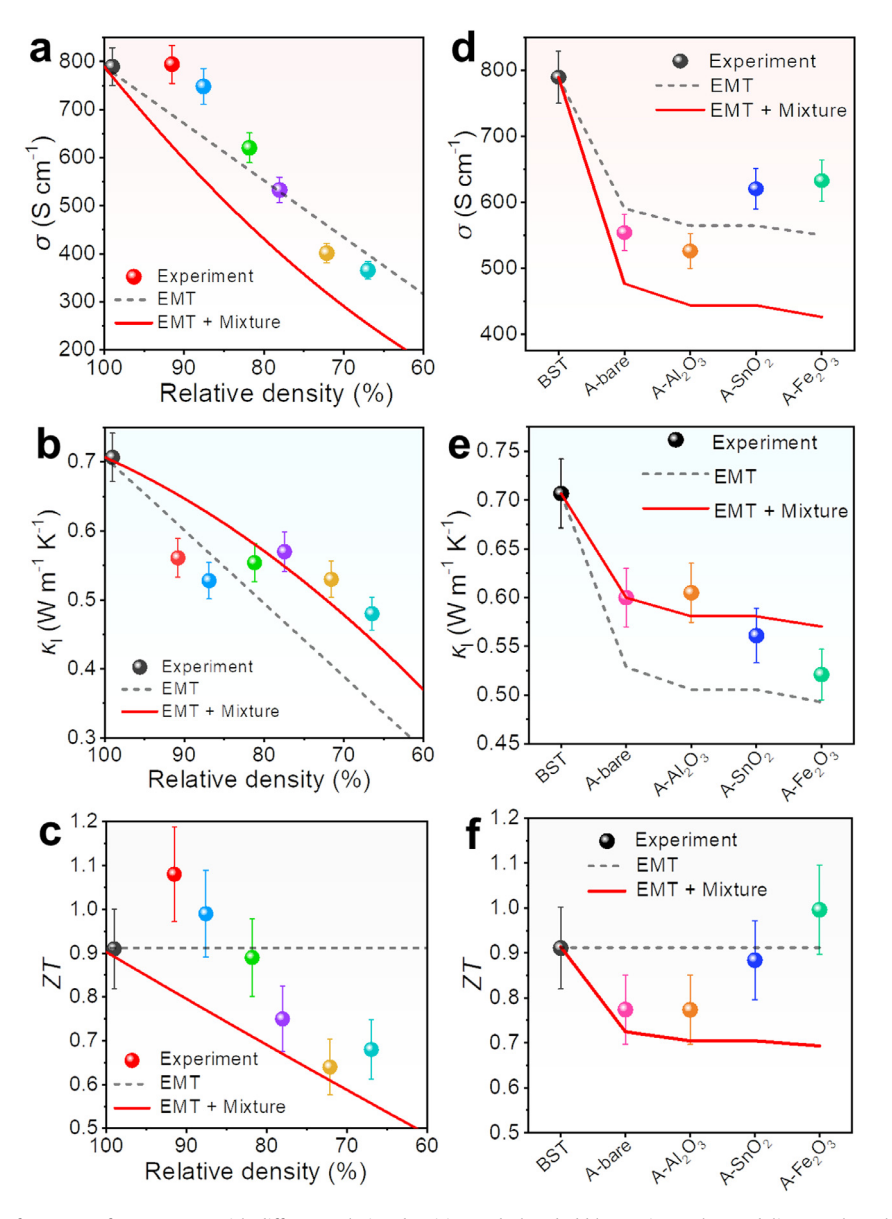


Fig. 6. Room-temperature TE performance of porous BST with different relative densities and glass bubble coatings. The modeling results calculated based on the EMT and EMT + Mixture model are provided for comparison. (a) σ , (b) κ_1 , and (c) ZT as a function of relative density when the coating materials are SnO₂, and (d) σ , (e) κ_1 , and (f) ZT of porous BST with glass bubbles coated with different oxides including bare (no coating), SnO₂, Al₂O₃, and Fe₂O₃ when the relative densities are all 80%.

where $\sigma_{\rm BST}$, $\sigma_{\rm com}$, and $\sigma_{\rm GB}$ are the electrical conductivities of the BST matrix, as-prepared composites, and glass bubbles, and f is the volume fraction of glass bubbles. By incorporating the EMT function, the above formula can be expressed as:

$$\sigma_{\text{com}} = (1 - 3\varepsilon/2) \left(\left(1 - f \right) \sigma_{\text{BST}} + f \sigma_{\text{GB}} \right) \tag{2}$$

The results based on the EMT + mixture are also provided in Fig. 6(a-c) for comparison. In samples with low glass bubble contents, the BST/glass bubble interface plays a significant role in the thermal and electrical transport properties of the entire composites, while the contribution of glass bubbles is counteracted. The experimental data exhibit notable deviations from the EMT + mixture results, primarily due to the contributions of the BST/glass bubble interfaces. For the samples with high glass bubble contents, the contributions of glass bubbles are dominated, and the experimental data should be gradually close to the EMT + mixture results, which is in accordance with experiment results, as shown in Fig. 6(a-c). The simultaneously high σ and low κ_1 are obtained for the sample with low glass bubble content. Typically, in the sample

with 1% glass bubbles, the introduced SnO_2 layer at the BST/glass bubble interface attributes $\sim\!29.2\%$ increment of σ and $\sim\!9.5\%$ reduction of κ_1 . For the sample with 1% glass bubbles, a high ZT of 1.08 at 300 K is obtained with a low relative density of $\sim\!91.5\%$, which is $\sim\!33.3\%$ higher than the EMT + mixture result.

Based on the above discussions, we further analyze the asachieved experimental results. As shown in Fig. 6(a), the experimental σ data of all samples are much higher than the EMT + mixture results, which could be ascribed to the contributions of the oxide layers on n_p and μ . This statement is confirmed by the experimental results that the n_p is increased from 3.3 to 3.5 \times 10¹⁹ cm⁻³ after introducing 1% coated glass bubbles. Moreover, many structural defects are formed at interfaces between the BST matrix and glass bubbles, which is beneficial for the increase of n_p because of the charge build-up at the interfaces. Also, the m^* value of the sample with low glass bubble content (1%, Fig. 5(e)) is even higher than that of the sample without glass bubble, which could be attributed to the multiple roles of the oxide layer including hole donors and potential barrier. Conversely,

the contributions of glass bubbles are dominated by the samples with high glass bubble contents. The significantly decreased $n_{\rm p}$ and μ shown in Fig. 5(d) result in much lower m^* values. Moreover, the nanoscale precipitates (such as the oxide layers at the broken glass bubbles) and strains at the BST/glass bubble interfaces would effectively scatter phonons with short and medium wavelengths. The grain boundaries can scatter the phonons with long wavelengths. Additionally, the BST/glass bubble interfaces can further scatter the phonons with long wavelengths due to the large radius and average distance of glass bubbles. Thus, in this work, the carrier/phonon transport behavior of the porous composites is optimized by introducing the ALD-prepared oxide bonding layers at the BST/glass bubble interfaces.

To evaluate the effects of nano-oxide bonding layers on carrier and phonon transport behaviors, the TE performance of porous BST with 3% glass bubbles without an oxide layer (A-bare), and porous BST with 3% glass bubbles coated with different metal oxide layers, including SnO₂ (A-SnO₂), Al₂O₃ (A-Al₂O₃), and Fe₂O₃

(A-Fe₂O₃), were measured, as shown in Figs. 6(d-f) and S7. The introduction of metal oxide layers has optimized the electrical and thermal transport properties of the porous BST. The comparatively higher σ and $S^2\sigma$ of A-SnO₂ compared to A-bare indicate that the SnO₂ layer can reduce carrier scattering at the interfaces between the BST matrix and glass bubbles. Moreover, the κ_1 of Abare surpasses that of A-SnO2 at 300-525 K, demonstrating that the SnO₂ layer enhances phonon scattering. Due to the increased σ and reduced κ_1 , the highest ZT of A-SnO₂ is approximately 16.3% higher than that of A-bare. These results reveal that the introduced metal oxide layers simultaneously contribute to higher σ and ultralow κ_1 , which is essential for optimizing the TE performance of porous BST. Fig. 6(d-f) and S8 show the experimental σ , κ_1 , and ZT of the porous BST with 3% glass bubbles coated with different metal oxide layers. The relative densities of all samples are \sim 80%, which ensures that the porosities of samples mainly depend on the glass bubble contents. As shown in Fig. 6(e), both the porosity and glass bubbles contribute to the decrease in κ_1 . By subtracting

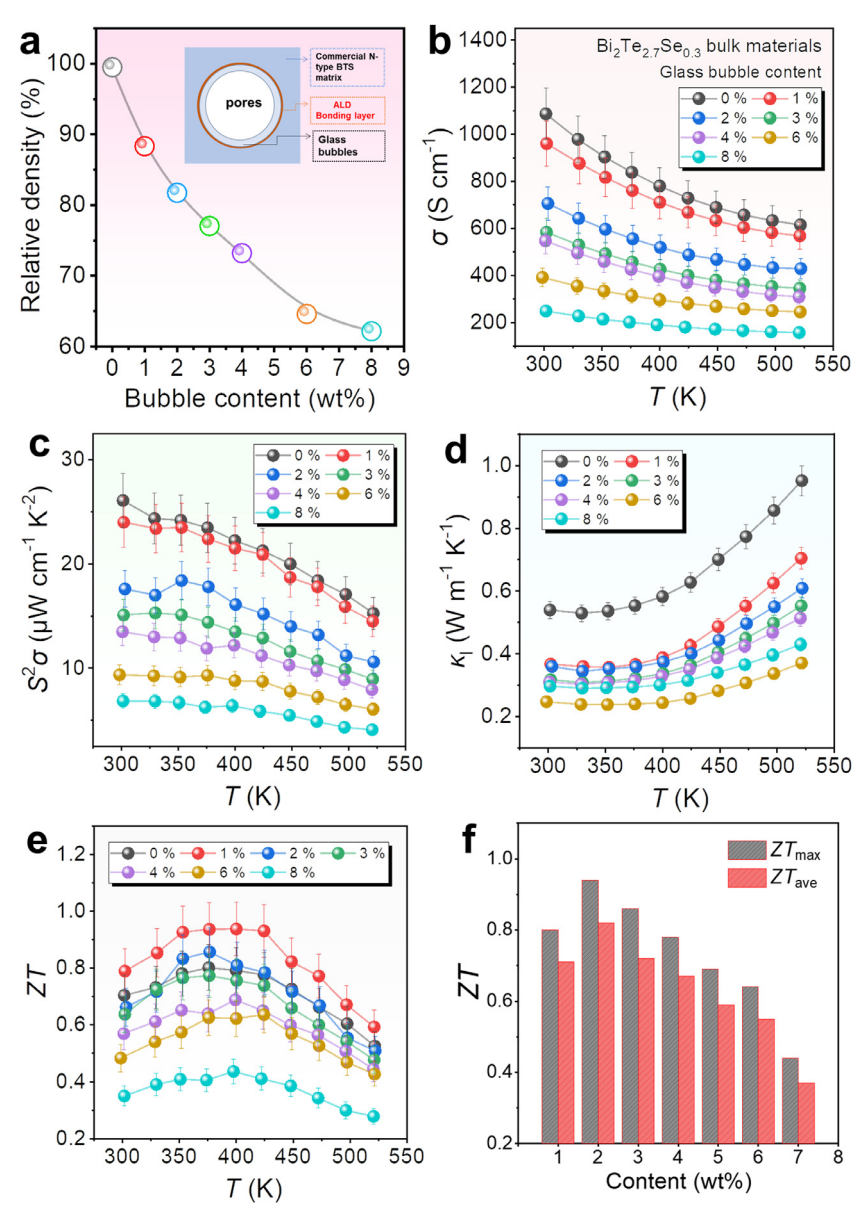


Fig. 7. TE performance of porous $Bi_2Te_{2.7}Se_{0.3~(BTS)}$) with different bubble contents (0%, 1%, 2%, 3%, 4%, 6%, and 8%). (a) Measured relative densities of porous BTS as a function of bubble content. The inset shows the structure of the coated glass bubble. Temperature-dependent (b) σ , (c) $S^2\sigma$, (d) κ_1 , and (e) ZT. (f) Maximum ZT (ZT_{max}) and average ZT (ZT_{ave}) of porous BTS as a function of bubble content.

the EMT+ mixture results from experimental data, the contribution of the metal oxides layer to the κ_1 could be estimated. For the A-bare sample, the experimental data are well consistent with the EMT+ mixture results, implying that the method is effective. A similar result could be obtained for the A-Al₂O₃ sample, which could be attributed to the high κ (~30 W m⁻¹ K⁻¹) as well as the low chemical activity of Al_2O_3 . However, an extremely reduced κ_1 could be observed for the samples A-SnO2 and A-Fe2O3. As mentioned above, the unique features including the metal oxides layer and intensive nanoscale crystalline regions of the interface may be beneficial for increasing thermal resistance and thus lowering the κ_1 . For the A-Fe₂O₃ sample, the porosity and Fe₂O₃ layer contribute to about 19.4% and 7.1% reduction of κ_1 , respectively. Moreover, a similar analysis is adopted to evaluate the effect of the metal oxides on the σ . As shown in Fig. 6(d), both the porosity and glass bubbles contribute to the decrease in σ . Thus, the contribution of the metal oxides could be obtained by subtracting the EMT+ mixture results from experimental data. Typically, for the A-Fe₂O₃ sample, the porosity and glass bubbles as secondary phases resulted in \sim 30.3% and \sim 15.7% reductions of σ , respectively. The Fe₂O₃ layer contributed to \sim 26.2% enhancement of σ .

As a result, the σ value of the A-Fe₂O₃ sample is \sim 14.2% higher than that of the A-bare sample, which further confirms that the Fe_2O_3 layer is crucial to improving the σ . Due to the reduced κ_1 and the enhanced σ , the room temperature ZT of A- Fe_2O_3 is ~47.4% higher than the EMT+ mixture results (Fig. 6(f)). The room temperature MQF value of A-Fe₂O₃ is approximately \sim 137.9 \times 10⁻³ K m³ V⁻¹ S⁻¹ W⁻¹, significantly surpassing that of the A-bare and porous BST materials [20]. As a result, the highest ZT reaches 1.06 at 350 K for the A-Fe₂O₃ sample, representing an impressive 23% improvement compared to the ZT of 0.86 at 350 K for the A-bare sample. Thus, the results reveal that the introduced metal oxide layers simultaneously contribute to the high σ and ultralow $\kappa_{\rm l}$, which is the fundamental reason for the high TE performance. The detailed temperature-dependent TE properties of porous BST with glass bubbles coated with different metal oxides are shown in Fig. S8, and their maximum ZT (ZT_{max}) values are compared in Fig. S9 for reference.

To verify that our porous design could be applied to other TE materials, we further fabricated the n-type porous BTS using the same fabrication route. The BTS/glass bubble composites were prepared by introducing SnO2 layers between the BTS matrix and the glass bubbles. As expected, with increasing the mass fraction of glass bubbles, the relative density of the as-prepared composites was decreased, as shown in Fig. 7(a). Fig. 7(b-e) shows temperature-dependent σ , $S^2\sigma$, κ_1 , and ZT of porous BTS with different bubble contents (0%, 1%, 2%, 3%, 4%, 6%, and 8%), while the temperature-dependent S and κ values are shown in Fig. S10 for reference. Similar to the results of porous BST, with increasing the bubble content, σ , $S^2\sigma$, κ_1 , and κ_1 were all decreased. However, when the bubble content is low (1%), the oxide bonding layers contribute to \sim 19.4% reduction of κ_1 and \sim 26.2% enhancement of σ . As a result, low-cost and high-performance porous BTS/glass bubble composites were obtained. Fig. 7(f) compares ZT_{max} and average ZT (ZT_{ave}) of porous BTS as a function of bubble content. A peak ZT of 0.94 at 400 K, as well as a ZT_{ave} of 0.82 between 300 and 500 K, is obtained for the sample with 1% SnO2-coated glass bubbles (${\sim}88.8\%$ relative density), which are ${\sim}17.5\%$ and ${\sim}15.5\%$ higher than that of commercial BTS without glass bubble, respectively. Thereby, these results confirmed the universality of this novel porosity design.

3. Conclusion

In this study, we incorporated glass bubbles into commercial BST to create thermoelectric materials that are both highly cost-

effective and efficient. Unlike traditional methods, we introduced metal oxide bonding layers at the interfaces between the BST matrix and the glass bubbles using an ALD technique. This approach helps to maintain high electrical conductivity (σ) and effectively reduce the thermal conductivity (κ_1) of the prepared porous TE materials. The resulting porous TE materials, which had a relative density of approximately 86.9%, achieved a high figure of merit (ZT) of 1.22 at 350 K. This represents a significant improvement of approximately 23.2% compared to the solid BST material, which had a ZT of 0.99 at the same temperature. We found that this strategy is universally effective and can be applied to design cost-effective and high-performance TE composites based on Bi₂Te_{2.7}Se_{0.3} (BTS). Considering the widespread use of glass bubbles and bismuth telluride in commercial applications, this approach is highly compatible with industrial practices and holds great potential for practical implementation.

Declaration of competing interest

The authors declare that they have no known competing financial interests or personal relationships that could have appeared to influence the work reported in this paper.

CRediT authorship contribution statement

Shuankui Li: Conceptualization, Data curation, Formal analysis, Funding acquisition, Investigation, Project administration, Supervision, Validation, Writing - original draft. Wenguang Zhao: Data curation, Formal analysis, Methodology, Software, Validation, Visualization, Writing - original draft. Xiao-Lei Shi: Data curation, Formal analysis, Resources, Software, Validation, Visualization, Writing - original draft, Liangliang Wang: Data curation, Formal analysis. Shusheng Pan: Data curation, Formal analysis. Guofeng Cheng: Data curation, Formal analysis. Wei-Di Liu: Software. Meng Li: Resources, Software. Kai Guo: Conceptualization, Funding acquisition, Investigation, Project administration, Supervision. Zhi-Gang Chen: Conceptualization, Data curation, Formal analysis, Funding acquisition, Investigation, Project administration, Validation, Writing - review & editing. Feng Pan: Conceptualization, Funding acquisition, Investigation, Project administration, Supervision, Writing - review & editing.

Acknowledgements

This work was financially supported by the National Natural Science Foundation of China (Nos. U21A2054, 21905007), and the Key Discipline of Materials Science and Engineering, Bureau of Education of Guangzhou (Grant No. 202255464). Zhi-Gang Chen thanks the financial support from the Australian Research Council, HBIS-UQ Innovation centre for Sustainable Steel project, and QUT Capacity Building Professor Program. Shuankui Li thanks the support from the exploratory experimental projects from Guangzhou University. This work was enabled by the use of the Central Analytical Research Facility hosted by the Institute for Future Environments at QUT.

Supplementary materials

The details on the experimental section, including materials synthesis and fabrication, characterization, and thermoelectric property measurement supplied in Supporting Information.

Supplementary material associated with this article can be found, in the online version, at doi:10.1016/j.jmst.2024.06.037.

References

- [1] X.L. Shi, J. Zou, Z.G. Chen, Chem. Rev. 120 (2020) 7399-7515.
- [2] B. Jiang, W. Wang, S. Liu, Y. Wang, C. Wang, Y. Chen, L. Xie, M. Huang, J. He, Science 377 (2022) 208–213.
- [3] Q. Yang, S. Yang, P. Qiu, L. Peng, T.R. Wei, Z. Zhang, X. Shi, L. Chen, Science 377 (2022) 854-858
- [4] G.J. Snyder, E.S. Toberer, Nat. Mater. 7 (2008) 105-114.
- [5] G. Tan, L.D. Zhao, M.G. Kanatzidis, Chem. Rev. 116 (2016) 12123-12149.
- [6] H. Sang, W. Wang, Z. Wang, M. Hong, C. Zhang, S. Xie, H. Ge, F. Yan, Z. Wang,
- Y. Ouyang, Y. Liu, J. Wu, W. Liu, X. Tang, Adv. Funct. Mater. 33 (2023) 2210213.
 [7] L. Pan, X.L. Shi, C. Song, W.D. Liu, Q. Sun, C. Lu, Q. Liu, Y. Wang, Z.G. Chen, Adv. Funct. Mater. 32 (2022) 2202927.
- [8] S. Li, X. Fang, T. Lyu, J. Cheng, W. Ao, C. Zhang, F. Liu, J. Li, L. Hu, Mater. Today Phys. 27 (2022) 100764.
- [9] L. Hu, B. Duan, T. Lyu, N. Lin, C. Zhang, F. Liu, J. Li, M. Wuttig, Y. Yu, Adv. Funct. Mater. 33 (2023) 2214854.
- [10] B. Yu, J. Duan, H. Cong, W. Xie, R. Liu, X. Zhuang, H. Wang, B. Qi, M. Xu, Z.L. Wang, J. Zhou, Science 370 (2020) 342-346.
- [11] Y. Pan, U. Aydemir, J.A. Grovogui, I.T. Witting, R. Hanus, Y. Xu, J. Wu, C.F. Wu, F.H. Sun, H.L. Zhuang, J.F. Dong, J.F. Li, V.P. Dravid, G.J. Snyder, Adv. Mater. 30 (2018) 1802016.
- [12] Y. Pan, Y. Qiu, I. Witting, L. Zhang, C. Fu, J.W. Li, Y. Huang, F.H. Sun, J. He, G.J. Snyder, C. Felser, J.F. Li, Energy Environ. Sci. 12 (2019) 624–630.
- [13] X.L. Shi, W.Y. Chen, X. Tao, J. Zou, Z.G. Chen, Mater. Horiz. 7 (2020) 3065–3096.
- [14] X. Shi, A. Wu, W. Liu, R. Moshwan, Y. Wang, Z.G. Chen, J. Zou, ACS Nano 12 (2018) 11417-11425.
- [15] B. Xu, T. Feng, M.T. Agne, L. Zhou, X. Ruan, G.J. Snyder, Y. Wu, Angew. Chem. Int. Ed. 56 (2017) 3546-3551.
- [16] X.L. Shi, W.D. Liu, M. Li, Q. Sun, S.D. Xu, D. Du, J. Zou, Z.G. Chen, Adv. Energy Mater. 12 (2022) 2200670.
- [17] C. Gayner, N. Nandihalli, Materialia 14 (2020) 100912.
- [18] W. Liu, X. Shi, R. Moshwan, M. Hong, L. Yang, Z.G. Chen, J. Zou, Sustain. Mater. Technol. 17 (2018) e00076.
- [19] K. Guo, J. Zhang, Y. Zhang, L. Liu, S. Yuan, Y. Jiang, J. Luo, J.T. Zhao, ACS Appl. Energy Mater. 4 (2021) 5015-5023.

- [20] S. Li, R. Wang, W. Zhu, M. Chu, Z. Huang, Y. Zhang, W. Zhao, F. Liu, J. Luo, Y. Xiao, F. Pan, Adv. Electron. Mater. 6 (2020) 2000292.
- [21] K.T. Kim, S.Y. Choi, E.H. Shin, K.S. Moon, H.Y. Koo, G.G. Lee, G.H. Ha, Carbon 52 (2013) 541-549.
- [22] R. Nunna, P. Qiu, M. Yin, H. Chen, R. Hanus, Q. Song, T. Zhang, M.Y. Chou, M.T. Agne, J. He, Energy Environ. Sci. 10 (2017) 1928-1935.
- [23] S. Li, Y. Liu, F. Liu, D. He, J. He, J. Luo, Y. Xiao, F. Pan, Nano Energy 49 (2018) 257-266.
- [24] S. Li, Z. Huang, R. Wang, C. Wang, W. Zhao, Y. Ni, F.S. Liu, J. Luo, Y. Xiao, F. Pan, J. Mater. Chem. A 9 (2021) 11442–11449.
- [25] S. Li, L. Wang, D. Ma, Y. Jiang, K. Guo, J. Luo, Mater. Today Phys. 39 (2023) 101287.
- [26] T. Lu, B. Wang, G. Li, J. Yang, X. Zhang, N. Chen, T.H. Liu, R. Yang, P. Niu, Z. Kan,
- H. Zhu, H. Zhao, Mater. Today Phys. 32 (2023) 101035. [27] B. Jiang, Y. Yu, J. Cui, X. Liu, L. Xie, J. Liao, Q. Zhang, Y. Huang, S. Ning, B. Jia, B. Zhu, S. Bai, L. Chen, J. Pennycook Stephen, J. He, Science 371 (2021) 830-834.
- [28] Y. Qin, B. Qin, T. Hong, X. Zhang, D. Wang, D. Liu, Z.Y. Wang, L. Su, S. Wang, X. Gao, Z.H. Ge, L.D. Zhao, Science 383 (2024) 1204-1209.
- [29] Z. Liu, N. Sato, W. Gao, K. Yubuta, N. Kawamoto, M. Mitome, K. Kurashima, Y. Owada, K. Nagase, C.H. Lee, J. Yi, K. Tsuchiya, T. Mori, Joule 5 (2021) 1196-1208.
- [30] J. Guo, J. Yang, Z.H. Ge, B. Jiang, Y. Qiu, Y.K. Zhu, X. Wang, J. Rong, X. Yu, J. Feng, J. He, Adv. Funct. Mater. 31 (2021) 2102838.
- [31] P.A. Zong, R. Hanus, M. Dylla, Y. Tang, J. Liao, Q. Zhang, G.J. Snyder, L. Chen, Energy Environ. Sci. 10 (2017) 183-191.
- [32] G. Yang, L. Sang, F.F. Yun, D.R.G. Mitchell, G. Casillas, N. Ye, K. See, J. Pei, X. Wang, J.F. Li, G.J. Snyder, X. Wang, Adv. Funct. Mater. 31 (2021) 2008851.
- [33] Y. Wang, M. Hong, W.D. Liu, X.L. Shi, S.D. Xu, Q. Sun, H. Gao, S. Lu, J. Zou, Z.G. Chen, Chem. Eng. J. 397 (2020) 125360.
- [34] I.T. Witting, J.A. Grovogui, V.P. Dravid, G.J. Snyder, J. Mater. 6 (2020) 532-544
- [35] J. Yang, H.L. Yip, A.K.Y. Jen, Adv. Energy Mater. 3 (2013) 549-565.
- [36] C. Gayner, Y. Amouyal, Adv. Funct. Mater. 30 (2019) 1901789.[37] X. Lu, Q. Zhang, J. Liao, H. Chen, Y. Fan, J. Xing, S. Gu, J. Huang, J. Ma, J. Wang, L. Wang, W. Jiang, Adv. Energy Mater. 10 (2020) 1902986.